ORIGINAL ARTICLE

Banding and microstructural features in laser cladding of a 304 substrate using 316 powder

Edwar A. Torres[1] · Luis H. R. Apolinario[2,3] · Helen R. Araujo[2,3] · Ivan B. M. Picchi[2,3] · Tiago F. A. Santos[2,3]

Abstract

The aim of the cladding process is to improve mechanical, chemical, and physical features of the surface of metals. This laser process is frequently used to promote such alterations via deposition of metals/alloys with mechanical behavior superior to that of the substrate. In this contribution, an AISI 304 austenitic stainless steel is covered with an AISI 316 as powder filler metal using multiple laser deposition parameters. In the produced samples, the effect of the studied parameters on the geometry, surface appearance, dilution, and microstructural features was evaluated. The authors focus on metallurgical characteristics of cladding, seeking to explain the formation of three attributes: banding, columnar structure, and equiaxial grains. It was determined that banding is composed of a cellular-dendritic structure and is generated by changes in the microstructure size, derived from local variations in the solidification rate. The same applies for the columnar and equiaxial zones, but the appearance of equiaxial geometry is due to the change of the growth direction of the aforementioned columns, in the middle of the fusion zone. All the samples confirmed the formation of F/MA-type solidification mode, which indicates that the cooling rate is low and similar to those recorded in conventional fusion welding.

Keywords Geometric features · Banding and microstructure formation · Constitutional supercooling · Solidification modes

1 Introduction

The 316 stainless steel is about 29% more expensive than 304 [1]. Moreover, 316 provides better pitting corrosion resistance, which makes it a preferable choice [2]. Consequently, AISI 316 austenitic stainless steels are often more suitable candidates for use as coatings on 304 substrates since they present satisfactory corrosion resistance in various types of environment, good impact properties at low temperatures, and reliable weldability when due care is taken. These materials are often used in applications that require corrosion resistance at high temperatures [3–5], such as in the petro-chemical and chemical industries, supporting structures, kitchen equipment, and medical products, among other applications.

Laser cladding is a metal deposition technique applied in coating deposition processes to protect parts from wear and/or corrosion, as well as to rebuild worn surfaces of expensive components. The deposition materials can be either powders or wires, which are fed directly into the laser-generated melt pool. In laser cladding with powder, the particles are injected into an inert carrier gas. The laser beam energy heats and melts some of the particles during the process. Some other particles melt when they strike the melt pool surface. These particles impinging on the melt pool form the clad deposition layer [6].

Although laser cladding promotes the enhancement of multiple material properties, hot cracking is a critical problem for Cr-Ni stainless steels, which can be minimized by inducing a certain amount of δ-ferrite in the as-welded microstructure. For austenitic stainless steels, there are four possible types of solidification and transformation of the solid state: solidification types A and AF are associated with the solidification of austenite as the primary phase, whereas types FA and F have ferrite as the primary phase [7–9].

✉ Tiago F. A. Santos

1 Department of Mechanical Engineering, Universidad de Antioquia, P.O. Box 1226, Medellin, AN, Colombia

2 Department of Mechanical Engineering, Universidade Federal de Pernambuco, Av. da Arquitetura, s/n, Recife, PE 50740-550, Brazil

3 Brazilian Institute for Material Joining and Coating Technologies (INTM), Universidade Federal de Pernambuco, Av. da Inovação, s/n, PE 50730-120 Recife, Brazil

The laser deposition parameters not only affect the shape of the deposited bead, but they also alter its chemical composition and microstructural evolution. For example, Goodarzi et al. [10] concluded that the laser power and speed control the width of the layer, while its height depends on multiple factors. Yu et al. [11] have shown that laser power controls the cladding width and has some influence on the layer height, but its main effect is on the dilution control. Recently, Yu et al. [12] stated that laser power increases the cladding width but reduces its depth and height, while the scanning speed has the opposite effect.

Furthermore, the chemical composition, dilution, and solidification rate significantly modify the microstructure in stainless steels, mainly during high speed and energy density fusion processes [13, 14]. The composition balance between ferrite-stabilizing elements and austenite-stabilizing elements (i.e., Cr/Ni-equivalent) is used to predict the solidification microstructures, such as residual δ-ferrite content, and the solidification modes. The phase transition from stable δ to metastable γ as the primary solidification phase has also been observed when solidification velocity increases [15, 16]. Due to the characteristics of this system, a complex microstructure is produced with mixed cellular and equiaxial dendrites [17] in which the presence of bands persists, whose development and conformation are not fully elucidated in stainless steels [18–20].

The aim of this work is to investigate the influence of the laser cladding process variables on the deposition layer geometric aspects, the band formation and its microstructural evolution using an AISI 316 coating on an AISI 304 base metal.

2 Materials and methods

AISI 304 stainless steel plates of 5.15-mm thickness were used as substrate. The plates were coated by laser using AISI 316 stainless steel as filler powder, with a particle size of 132 ± 11 mm. The chemical composition of both metals was measured by arc spark optical emission spectroscopy (OES), using five replicas of each material. The measured compositions are shown in Table 1.

The laser classing process was performed using a Yb fiber laser operating in continuous wave mode. The filler powder was fed axially relative to the laser beam to produce deposition beads with 36 mm in length. The laser beam parameters

Table 2 Laser beam parameters for the deposition of AISI 316 powder on AISI 304 substrate

Parameter	Laser power (W)	Laser speed (mm/s)	Turntable (%)
1	1000	15	15
2			20
3		20	15
4			20
5	1200	15	15
6			20
7		20	15
8			20

are shown in Table 2, where the variable factors were the laser power, laser scanning speed, and the powder feeder (turntable), keeping constant the stirrer (20%), protection gas flow (5 l/min), powder transport gas flow (7 l/min), and laser focus (25 mm).

The effect of each parameter was evaluated considering the dilution, which was calculated using Eq. 1. With these results, and using the diagram WRC-1992, Cr_{eq}/Ni_{eq} ratios were calculated for each set of deposition parameters.

$$\%D = \frac{A}{A+B} \times 100 \tag{1}$$

Microstructural characterization of the coated samples was performed using optical microscopy (OM) and scanning electron microscopy (SEM). The samples were prepared in accordance with the ASTM E3-01 standard [21], by grinding with wet sanding and polishing with diamond paste up to 1 μm. The microstructure was revealed using two chemical etchants: aqua regia (HCl:HNO$_3$ = 3:1) for 40 s, and a solution of ferric chloride hexahydrate, water, and hydrochloric acid (50 mL HCl, 100 mL H$_2$O, and 5 g FeCl$_3$·6H$_2$O) for 3 min.

## 3 Results and discussion

3.1 Macrostructure and deposit shape

Figure 1 shows the macrographs of the eight deposited samples obtained with the parameters in Table 2. The dimensions and microstructure notably vary with the processing

Table 1 Chemical composition of the base metal and the coating powder

(% wt)	C	Si	Mn	P	S	Cr	Ni	Mo	Cu	Nb	Ti	V	Fe
Substrate AISI 304	0.05	0.364	1.50	0.024	0.01	17.76	8.04	0.242	0.346	0.039	0.008	0.084	Bal.
Coating AISI 316	0.072	0.68	1.55	0.0235	0.017	17.93	11.8	2.595	0.069	-	-	-	Bal.

Fig. 1 Macrographs of the cross section of the eight deposition cases, from sample 1 (**a**) to 8 (**h**). The etching was performed using aqua regia
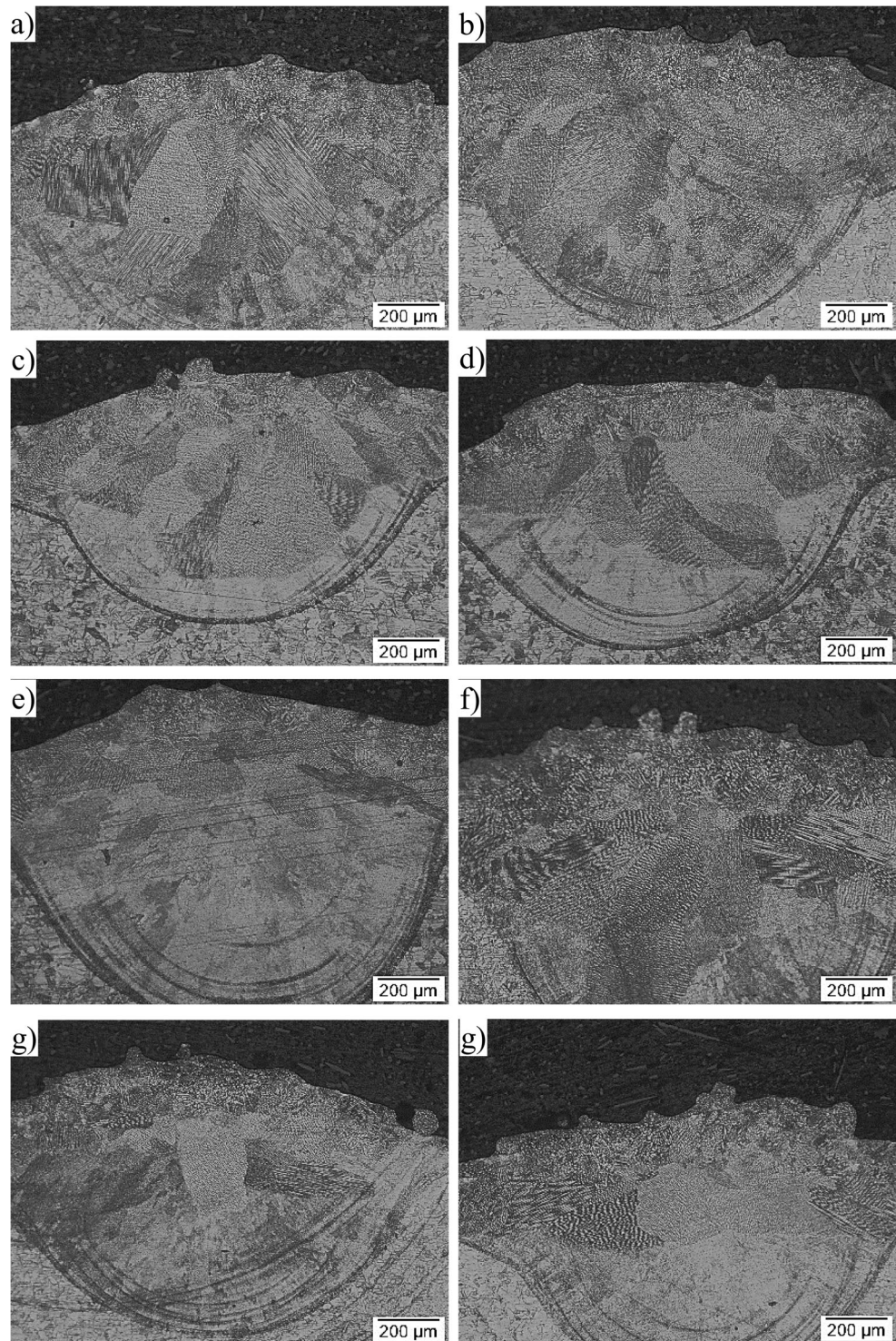
parameters. An important factor is the depth of the coating, which in principle must be low to reduce dilution and ensure the production of a layer with characteristics closer to the filler metal instead of the substrate metal [22].

As Fig. 2a shows, the penetration does not exceed 0.7 mm, which is considered low compared to the results presented by

Davim et al. [23], where the deposition depth in a 100 Mn Cr W4 (DIN) steel was 1.7 mm. Davim et al. [24] note that the penetration depends mainly on the power of the laser beam, as well as on the mass flow. About the latter, Riveiro et al. [25] underline the importance of mass flow and explain that when it increases, the depth of the coating decreasesdth because the
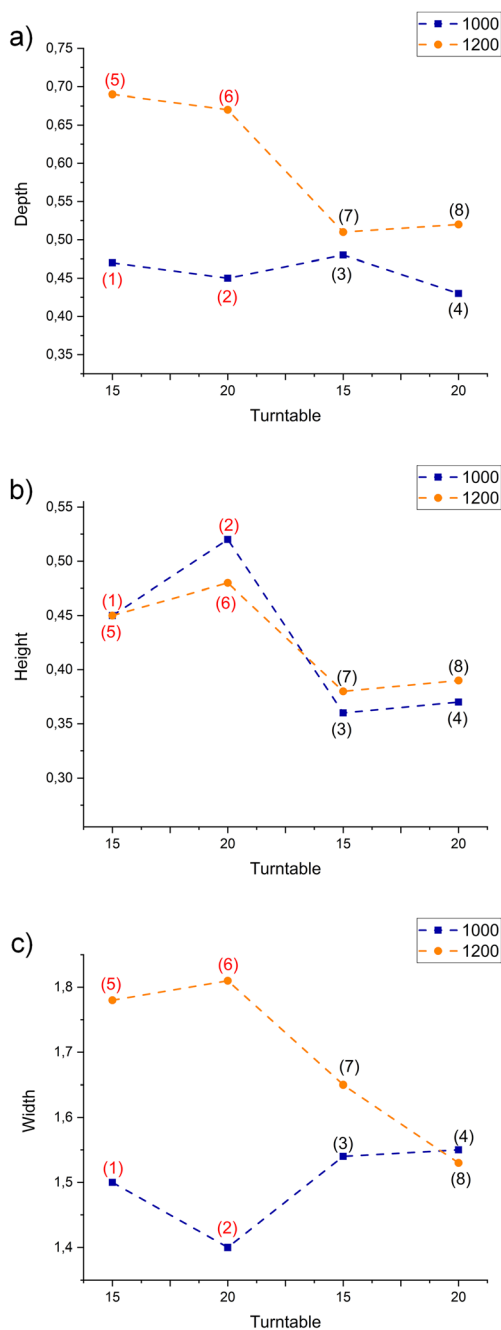
Fig. 2 Effect of the studied cladding parameters on the **a** depth, **b** height, and **c** width of the bead. The colors of the lines represent the laser power (1000 and 1200 W), and the numbers in parenthesis indicate the laser speed (red for 15 mm/s and black for 20 mm/s)

filler powder attenuates the laser radiation. As a result, the available energy to melt the substrate decreases due to the increase in the powder mass flow. In the same way, an increment in the scanning speed reduces the clad depth due to the decrease in the linear energy supplied to the substrate. The results in Fig. 2a agree with the observations of Davim et al. [24] and Riveiro et al. [25] concerning the proportional effect of the beam power, turnable, and scanning speed parameters.

Notably, sample 3 shows an unexpected increase in penetration, which could be explained by the impingement effect of the metal [26].

Furthermore, the behavior of height (Fig. 2b) and width (Fig. 2c) of the bead deposition agrees with the observations reported by Quin et al. [26] and Ju et al. [27]. Regarding the height, there is a crucial effect of turntable and power of the beam, because both allow an increase in the fusion rate and a metal accumulation when such parameters are high, and the laser velocity is low. Finally, when the scanning speed is low, the width depends primarily on the laser power.

Besides, the superficial aspect of the face reinforcement is heterogeneous since it reveals the presence of particles not fully incorporated in the coating. Oliveira et al. [28] explain that this effect depends on the laser power needed to melt the particles (P_{mp}), which in turn varies directly with the speed of the particle. This speed is defined through the powder transport gas flow, which, from the observable results, can be considered high.

3.2 Banding in the fusion zone

There are similar microstructural elements among the deposits, which stand out in Fig. 3. First, the formation of banding (Fig. 3a), and second, the presence of two regions in the fusion zone: a central zone with apparently equiaxial grains (Fig. 3b), lighter in the micrograph of Fig. 3a, and a region that extends from the fusion line (FL) to the center, darker in Fig. 3a. Both regions are well defined in all samples.

Concerning banding formation, Fig. 4a shows several lines near the FL. Banding is a phenomenon which has been observed at relatively low solidification speeds in welded or laser-treated materials. The formation of the so-called banded structure, consisting of a regular succession of dark and light bands, which has been found by several authors in rapidly solidified alloys [29].

For example, in the work of Peng et al. [30] about direct laser fabrication (DLF) in Ni-alloys, researchers determined that banding is a consequence of the grain size, with the grains in the light zones being much smaller than those in the dark zones. Zhang et al. [31] observed the same features in the laser deposition of 316 stainless steel on A36 structural steel, with the same differences in the substructures sizes of the light and dark bands. However, banding could be produced by distinct processes. Depending on the mechanism of their formation, the two alternating bands may consist of (1) different scales of the same microstructure, (2) periodically varying composition, (3) different microstructures of the same phase, (4) different phases, or (5) different phases and microstructures [32]. Gremaud et al. defined that a banded structure is composed of precipitation free α-Al solid solution, alternating with a dendritic structure [33].
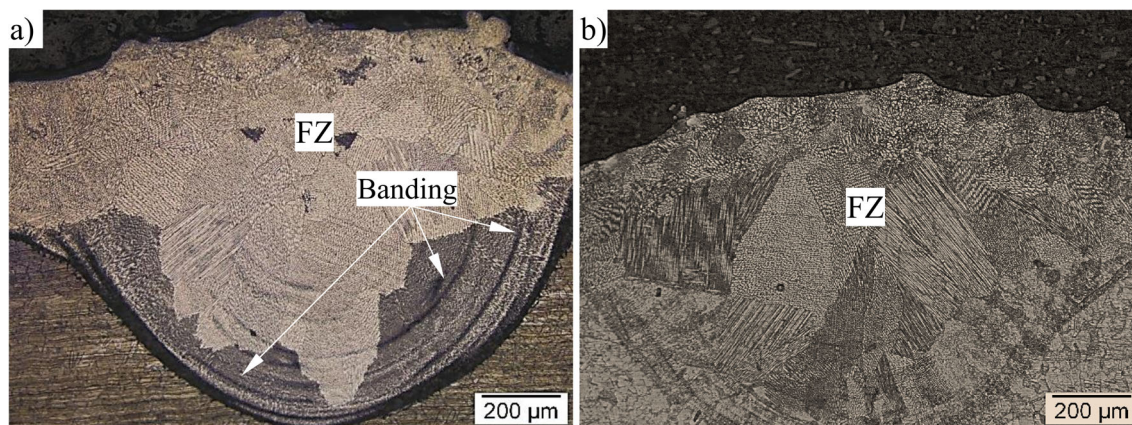
Fig. 3 Macrographs showing similar features of the coating microstructure: **a** sample 1 treated using ferric chloride, exhibiting the fusion zone (FZ) and banding, and **b** sample 1 treated using is aqua regia

Nonetheless, the most observed mechanisms in the laser process are 1 and 3. At low growth velocities, bands of the same microstructure but with different scales (mechanism 1) form through periodic fluctuations of the solidification system [32]. On the other hand, a banded structure in which two microstructures are formed (planar front and dendritic/cellular), corresponding to mechanism 3, have been observed at high scanning rates, in the regime between cellular/dendritic and planar front solidification [33]. In the present study, the banding mechanism corresponds to mechanism 1, due to changes in the microstructure size (Fig. 4b).

Bands have been observed in alloys with cellular/dendritic and eutectic microstructures, where the primary spacing (λ) of the dendritic structure is defined by Eq. 2 [34]:

$$\lambda^2 . R = \text{constant} \tag{2}$$

Therefore, the shift in the scale of the microstructure involves the variation in the solidification rate. All the samples show the first line of bands close to the FL, as revealed in Fig. 4. The structure is produced by epitaxial growth at the solid-liquid interface, a place where is registered an ultra-high temperature gradient (G) and a low solidification rate (R) due to

the process features. A columnar structure with epitaxial growth occurs in the bottom area, from the adjacent melted substrate. Because R is low, it promotes the formation of a microstructure with high λ, altered by growth rate fluctuations due to convection. The convection resulted in a slight increase of R and the consequent reduction of λ, producing the lighter region in the macrostructure.

3.3 Columnar and equiaxial grains in the fusion zone

Related to the presence of the lighter and darker regions, Zhong and Liu [35] sign that the solidification structure is characterized by columnar and equiaxed grains at the bottom and on the top, respectively. The first is due to the ultra-high G and low R at the fusion line, showing the typical directional solidification feature. Figure 5 shows the growth of the columnar structure from the FL toward the surface of the deposition bead, which coincides with the direction of the maximum temperature gradient.

On the top zone of the melt pool, columnar grains stopped growing while equiaxed grains arose due to the lower G and higher R local conditions. The same conclusions were
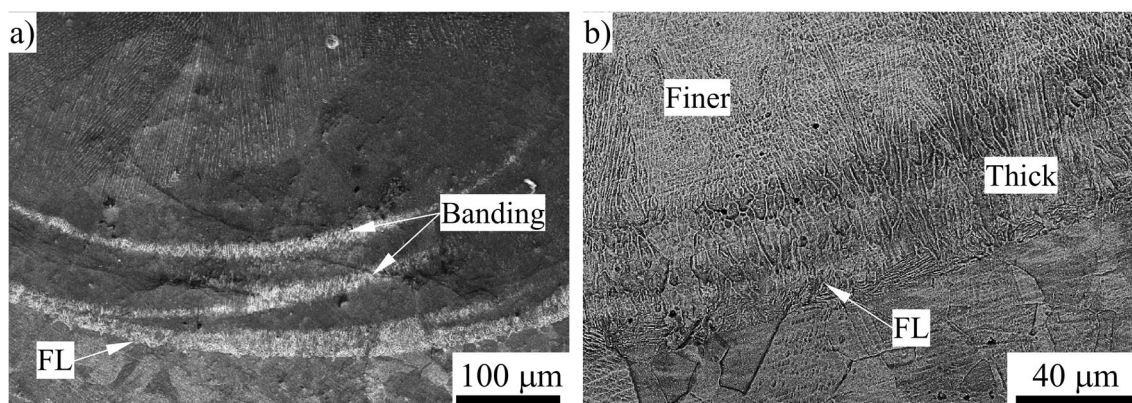

Fig. 4 a SEM image showing banding in sample 1. **b** Fusion boundary in sample 8, showing epitaxial growth (etched using ferric chloride)
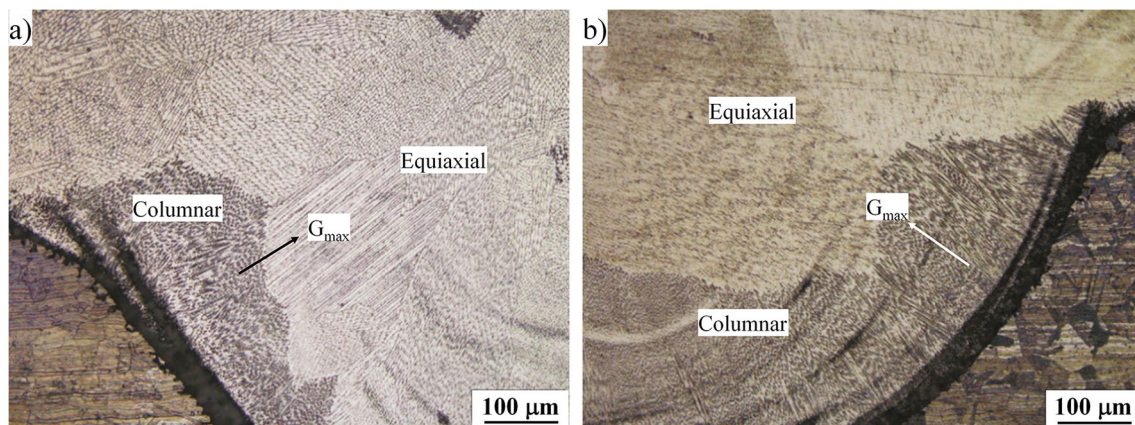
Fig. 5 OM images of **a** sample 1 and **b** sample 3, evidencing a columnar structure aligned with the growing direction (indicated by the arrow), toward G_{max} (etched using ferric chloride)

presented in a previous work [17], where the formation of a granular microstructure in the welding pool was explained based on the theory of columnar-to-equiaxial grain transition (CET). This theory attributes the granular microstructure to the particles detached from the columnar region, which could grow rapidly due to the high cooling rate, as argued by Hemmati et al. [36] based on the nucleation of particles due the constitutional supercooling. This could be represented in the solidification parameter (G/R) since the faster solidification rate (R), obtained at higher cladding speeds, supported the constitutional supercooling.

This interpretation agrees with the traditional view that explains the microstructural evolution in the welding fusion zone, which states that the microstructure depends on the chemical composition of filler metal and on the relationship between G and R, termed the solidification parameter (G/R), as summarized by David and Vitek [37]. As Koseki [38] point out, this theory applies to several processes involving metal

solidification. However, the generated microstructures depend on G and R, which are linked to the features of the process. For example, for arc welding and laser processing, G ranges from 10^4 to 10^5 K/m, and 10^5 to 10^7 K/m, respectively, while R varies between 10^{-5} to 10^{-2} m/s and 10^{-5} to 10 m/s, respectively [37]. Therefore, some differences are expected.

However, the reasonable interpretation that the microstructure in the middle region is formed by equiaxial grains would depend on the generated substructure: in the case of dendritic equiaxial substructure, the interpretation fits with what was previously described. Nevertheless, the observations show that grains near the CET and in the middle of the FZ have an elongated substructure, which would correspond to cellular or cellular-dendritic substructure (Fig. 6). In this situation, the traditional theory does not agree very well with the formation of such a structure.

Frenk and Kurz [39] evaluate the microstructure in laser-treated alloys considering the traditional microstructure approach, controlled by the G/R parameter, but considering that
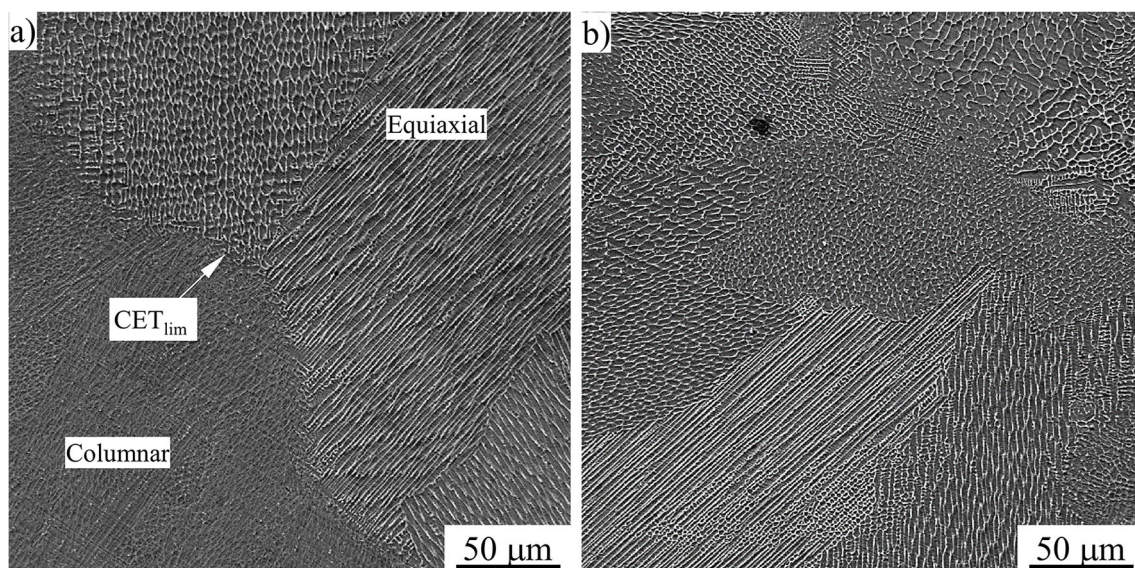

Fig. 6 SEM images showing the substructure of the grains in the middle of the deposits: **a** sample 3, near the boundary of the CET (CET_{lim}), and **b** sample 4, in the center of the deposited bead (etched using ferric chloride)
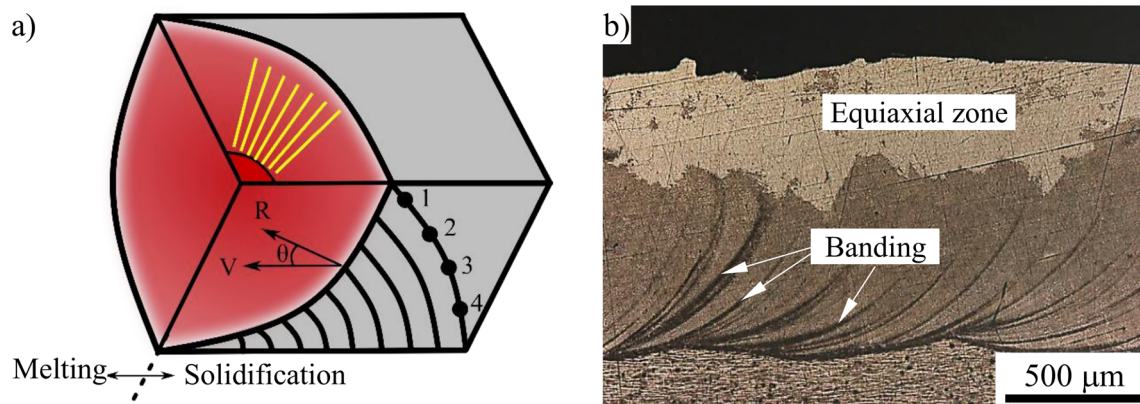
Fig. 7 **a** Scheme of changes in the solidification rate (R) as a function of laser beam velocity for remelting metals in laser cladding. **b** Macrostructure of the longitudinal cross-section on deposit 5 (etched using ferric chloride)

R changes as presented in Fig. 7. Figure 7a corresponds to the remelting process, where the energy of the beam melts the surface of the metal to promote its microstructure alteration. Curved lines symbolize the R changes, depending on the position in the fusion metal. Figure 7b illustrates the macrostructure of a long cross-section view on deposit 5, where the banding region is also observed.

In the solidification scheme of Fig. 7a, the solidification rate is lower at point 4, while it is maximum on the surface. The solidification direction is represented by the arrow in R. Thus, in the lower region, the microstructure grows in a nearly perpendicular fashion, while on the surface the microstructure stays almost parallel to the direction of the beam. This implies that in a cut perpendicular to the advance direction of the laser (Fig. 3a), the grains at the bottom of the bead have a columnar growth from the FL toward the surface, while those in the middle and surface regions appear to be equiaxial. However, in reality, they have the same columnar structure, but observed from the front and not the side.

Pei et al. [40] sign that in the laser cladding process the solidification rate and the beam speed could be related by Eq. 3, where θ is the angle between R and v (Fig. 7).

$$R = v . cos\theta \qquad (3)$$

Therefore, it is to be expected that just as the size of the deposit varies with power and scanning speed, the size of the equiaxial zone also changes, but in different proportions. Figure 8 relates the effect of power and laser scanning speed on the size of the equiaxial zone. Comparing Fig. 8a and c to Fig. 8b and d, it is obvious that the increase in laser power generates larger deposits but reduces the size of the equiaxial zone, which goes from 77.6 to 45.5%. This effect could be a consequence of the more intense fusion of the substrate since the laser speed was kept unchanged. This leads to an increase in angle θ with penetration, favoring the competitive growth of columnar grains formed at the solid-liquid interface.

Furthermore, comparing Fig. 8a and b to Fig. 8c and d, it is observed that increasing the laser speed from 15 to 20 mm/s reduces the size of the deposit and of the equiaxial zone. An explanation is that the increase in laser speed reduces significantly the θ angle, favoring the growth of grains parallel to deposition's direction.

3.4 Microstructural features in the fusion zone

In the fusion zone, the presence of banding and the columnar and equiaxial regions were macroscopically defined, as previously explained. Nevertheless, on a smaller scale, the structures that form the columnar and equiaxial grains were not yet revealed. Figure 9a shows the columnar zone (representative of all specimens) where cellular (Fig. 9b) and cellular dendritic (Fig. 9c) substructures are also present. Alloy solidification generally produces cellular or dendritic microstructures. These structures are characterized by microsegregation patterns which depend on the cell/dendrite morphology and spacing [41]. The presence of both microstructures was reported by Katayama and Matsunawa [42] in re-solidified 310S steel, with the formation of 100% austenitic cells with less than 2 μm in size, which was attributed to the high cooling rate (1500 °C/s). This result is very different from what occurs at slower cooling rates. Slower rates promote the formation of a duplex structure that when furnace-cooled (0.17 °C/s) promotes lacy ferrite and intercellular ferrite formation. Meanwhile, GTAW welding (220 °C/s) produces intercellular eutectic ferrite, observed at austenite grain and cellular dendritic boundaries.

Rapid solidification covers the range of growth velocities from 10^{-2} to 10^3 m/s, where the most important variable is the interface growth rate (R). In this work, and as defined by Eq. 3, the maximum growth rate ranged from 1.5×10^{-2} to 2.0×10^{-2} m/s, in the lower limit of the rapid solidification range.

Fig. 8 Processed images used to determine the effects of power and laser speed on the size of the equiaxial zone (in blue): **a** sample 1, 1000 W, 15 mm/s; **b** sample 3, 1000 W, 20 mm/s; **c** sample 5, 1200 W, 15 mm/s; and **d** sample 7, 1200 W, 20 mm/s
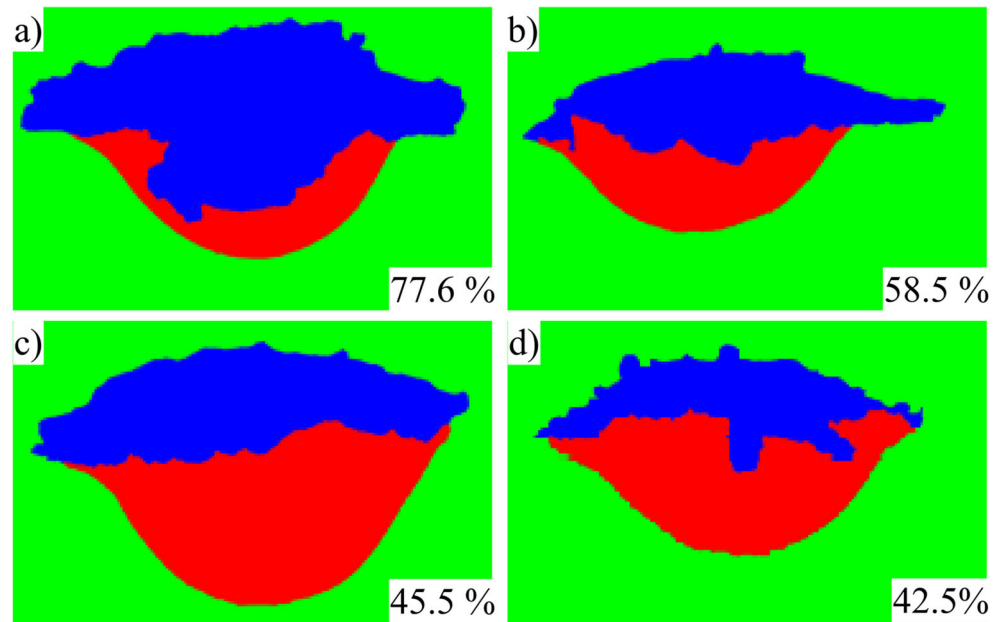
In laser treatment, R increases rapidly from zero at the bottom to a value close to the beam rate at the surface [43]. The temperature gradient (G) is highest at the bottom and decreases with thickness. Thus, in laser re-solidification, the G/R ratio is infinite at the bottom of the melt pool, promoting planar growth. Zhang et al. [31] reported the formation of a white
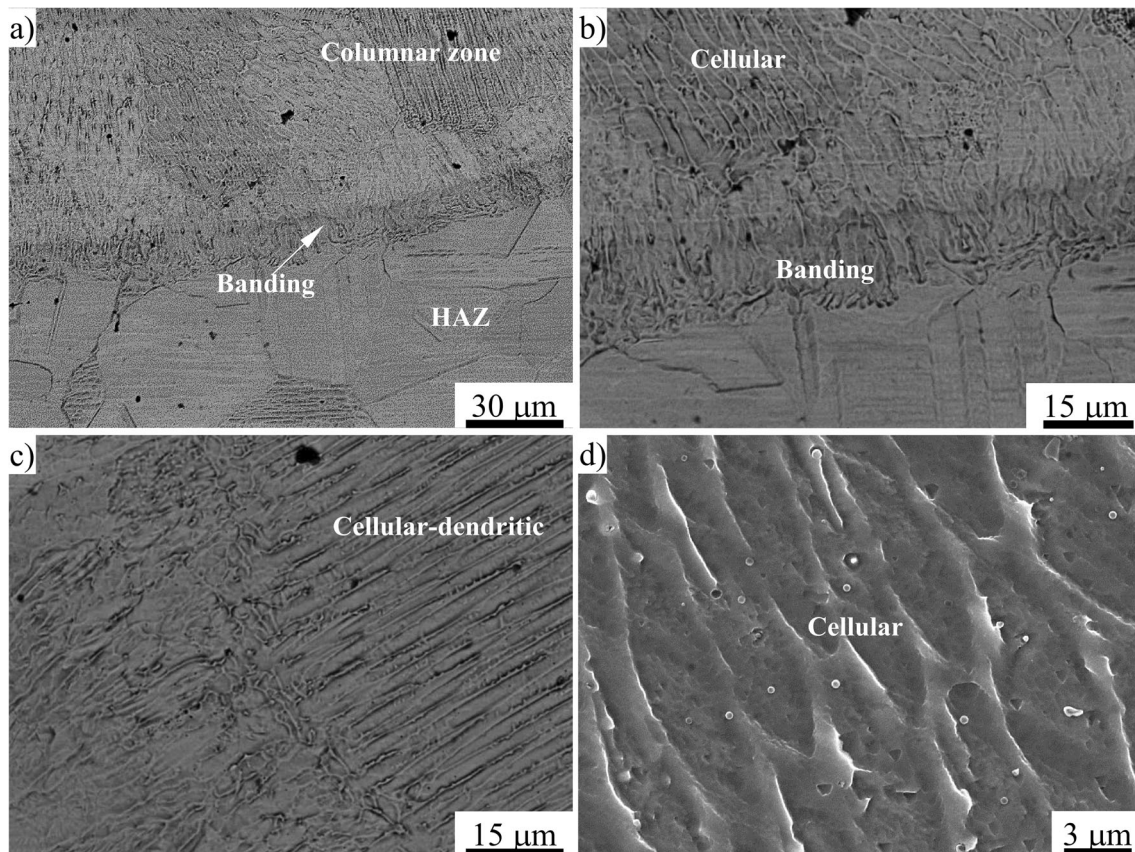

Fig. 9 SEM images of the columnar zone structure in sample 2: **a** melting line showing internal grain structure, **b** detail showing cell formation as solidification substructure, **c** evidence of cell-dendritic structure formation, and **d** detail of the cells in the columnar zone. Samples were etched using ferric chloride

bright band, which matches with the formation of a planar interface growth. Cell formation is related to a low solute amount or a high G/R, but lower than the needed to assist the formation of a planar solidification, which explains the presence of a cell structure near the fusion line [42]. The generated cells are thin, smaller than 5 and 15 μm in width and length, respectively (Fig. 9c). The existence of a cellular-dendritic structure means a change in chemical composition or a reduction in G/R ratio, with the latter being the most likely reason.

The equiaxial zone presents cellular, cellular-dendritic, and columnar dendritic substructures (Fig. 10). Also valid in this region is the principle described for the columnar zone, ruled by the constitutional supercooling, which is described by G/R and the cooling rate (G.R) [44]. Both are noted in the Fig. 10, where the microstructural alterations manifest from the bottom toward the top of the deposited bead. G/R growth decreases from the bottom toward the surface (where G/R is lower), which suggests that constitutional supercooling is greater on the surface, promoting the formation of columnar dendrites. In the middle and bottom, the constitutional supercooling is

weaker, ensuring the presence of slower solidification growth microstructures like cellular and cellular-dendrites.

Similar observations are described by Blecher et al. [45] in the fusion zone in nickel-chrome alloys, with the formation of cells spaced apart about 3 μm on the bottom, and columnar dendrites near the center with dendrite arm sizes from 4 to 5 μm. They consider a laser power of 1.0 kW and calculated G/R and G.R parameters, from the surface up to a 2 mm depth, of $0.5–10^3$ K s/mm² and $400–10^5$ K/s, respectively. Clearly, G/R and G.R increase with depth, similar to what is observed in Fig. 10. Blecher et al. [45] define a G/R contour of 13 K s/mm² as the transition value from cellular to columnar dendritic morphologies. Therefore, at values lower than 13 K s/mm², the morphology is likely to be dendritic.

The effect of G.R on the structure size is evident: the size of the cells in Fig. 10d (3 μm) is smaller than those shown in Fig. 10b (6 μm), indicating that the former experienced a faster cooling (G.R lower). Blecher et al. [45] indicate that the cell spacing ranges from 3.9 μm at 8000 K/s to 1.7 μm at 90,000 K/s, where the relationship between microstructure size and cooling rate is defined by Eq. 4.

Fig. 10 SEM micrographs of sample 1 reveling the substructure in the equiaxial zone and their evolution from the bottom to the top of the deposit. The arrow indicates the increase direction of the solidification parameter (G/R) and the cooling rate (G.R). Samples etched using ferric chloride
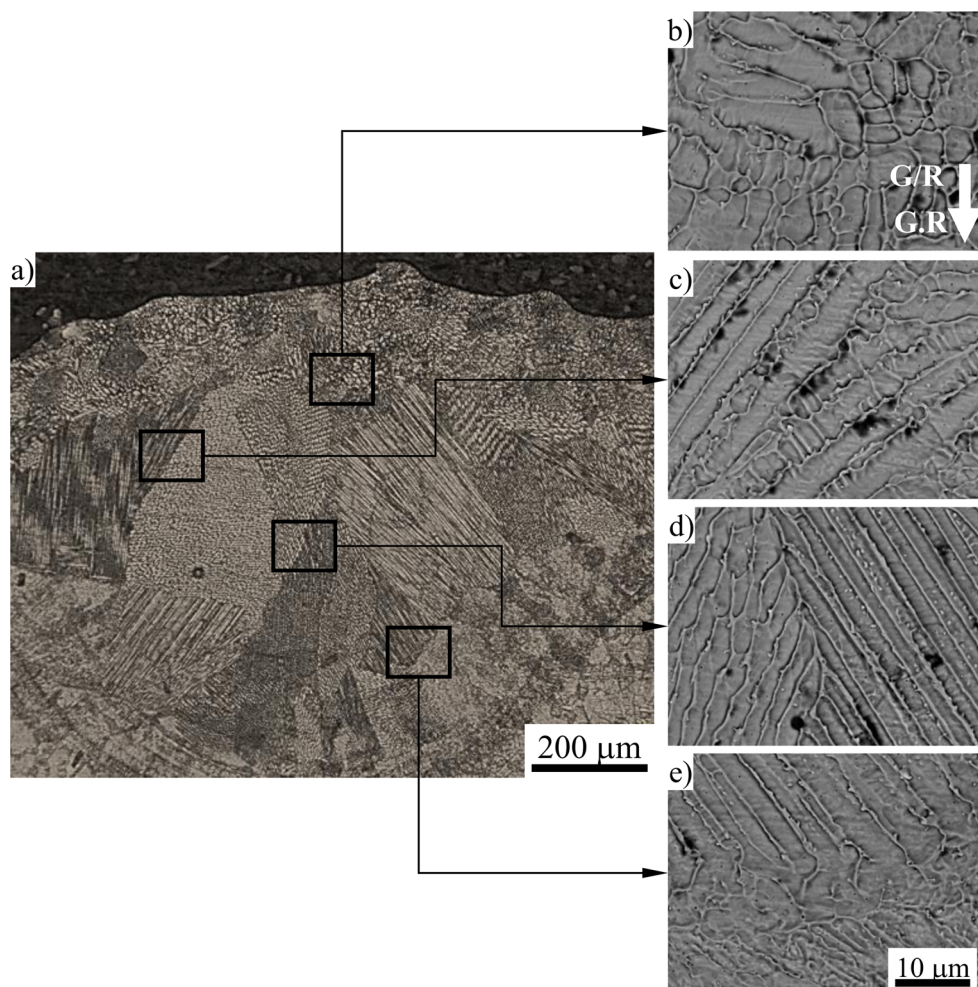
$$\lambda = b(G.R)^n \qquad (4)$$

3.5 Solidification mode

The OM images of the samples etched using ferric chloride solution presented lighter and darker regions, related to the types of phases in the sample. Since ferric chloride preferentially attacks the ferritic phase, the darker phase in the Fig. 3a and Fig. 5a is ferrite.

In conventional welding processes, the expected microstructure in the fusion zone could be conservatively predicted by the Schaeffler diagram, based on the chemical compositions of the substrate and the filler metal. Nonetheless, a more accurate approximation can be achieved using the diagram WRC-1992, shown in Fig. 11 [47]. For stainless steel single layer clad by GMAW, Shahi and Pandey determined the optimal dilution in 20% [48], while Yogananth et al. set it in 10% [49]. The Cr_{eq} and Ni_{eq} for substrate (18% and 9.8%) and metal power (20.5% and 14.3%) were measured from Table 1. Moreover, with a dilution mean value of 15% and using the WRC-1992 diagram, the formation of a duplex-type microstructure in the fusion zone can be predicted, with 3 to 4% of ferrite and primary ferrite solidification with second-phase austenite (FA). For such conditions, the ferrite microstructure could be of the interdendritic type, vermicular (skeletal), or lathy (Lacy) [2], as predicted and observed by Murugan and Parmar [50] in a cladding deposited on stainless steel by GMAW-A.

However, in the laser process, the phenomenon is different. David et al. [51] describe how the cooling rate changes the microstructure in 304 and 316 stainless steels, due to the fact
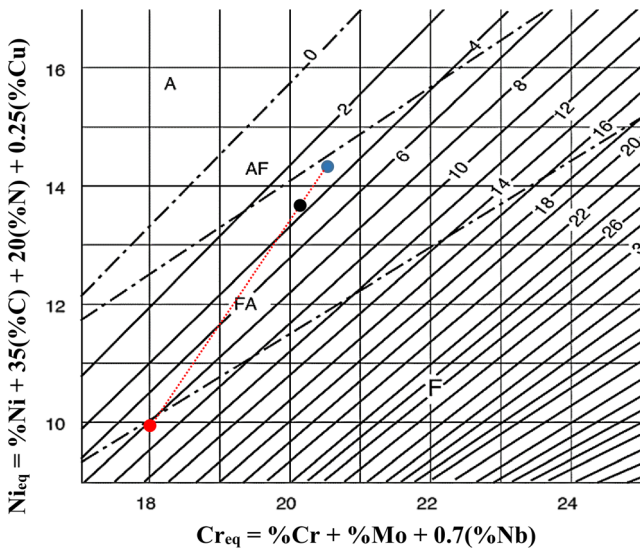
Fig. 11 WRC-1992 diagram indicating the microstructures of the substrate (red), the filler metal powder (blue), and the fusion zone (black), according to the Ni_{eq} and Cr_{eq} for filler and base metals and a dilution of 15% in the fusion zone. Adapted from [46]
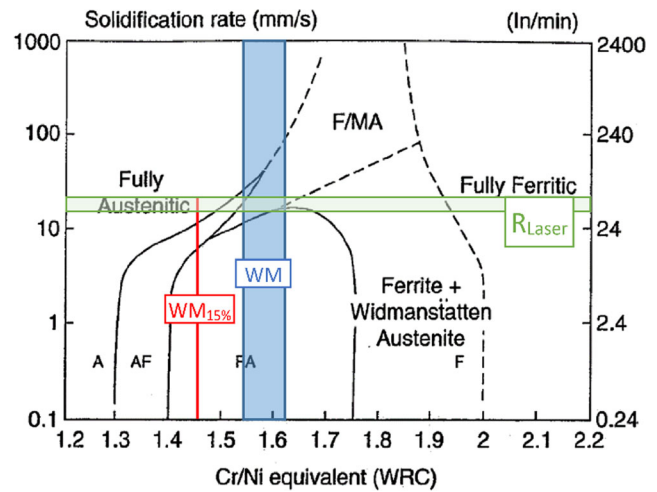
Fig. 12 Microstructural map showing the effect of chemical composition and solidification rate on the final microstructure in austenitic stainless steels. The red line is the Cr/Ni equivalent ratio of the fusion zone with a dilution of 15%. The blue region describes the dilution range measured in the laser cladding samples, and the green band denotes the range of solidification rate for the laser process. Adapted from [2, 3]

that solidification rates and postsolidification cooling rates have a profound effect on the produced microstructures, by favoring a reduction in the ferrite formation.

Such phenomena were confirmed in several stainless steels by Elmer et al. [52]. Lippold [4] has suggested explaining the formation of hot cracking in austenitic stainless steel through the development of a microstructural map as a function of solidification rate (R) and the WRC Cr_{eq}/Ni_{eq} ratio, as shown in Fig. 12. Authors like Frenk and Kurz [39] defined R values of 200 to 2000 mm/s, very different from the values established by Kurz and Trivedi [43], that covers the range of growth velocities from 10 to 1000 mm/s. As stated earlier in this work, the maximum growth rate varies from 1.5×10^{-2} to 2.0×10^{-2} m/s, which is the considered range represented in Fig. 12.

With these values, and for the 15% dilution ($WM_{15\%}$), Fig. 12 indicates the formation of a fully austenitic structure. However, the 15% dilution is an approximation. Therefore, the dilution was measured and, with Fig. 11, the Cr_{eq}/Ni_{eq} of each deposit was determined. The results of the different deposition conditions are provided in Table 3. With these results, the region in blue (highlighted vertical range identified by WM) is defined in Fig. 12, which outlines the dilution in the

Table 3 Results of the measured dilution and calculated Cr_{eq}/Ni_{eq} ratio for the different deposition conditions using the WRC-1992 diagram

Condition	1	2	3	4	5	6	7	8
Dilution (%)	43	31	48	45	51	44	54	44
Cr_{eq}/Ni_{eq}	1.58	1.54	1.60	1.59	1.61	1.58	1.62	1.58

different samples and predicts the F/MA solidification in all samples, agreeing with the observations of Apolinario et al. [17]. Elmer et al. [46] reported that in stainless steels high cooling rates favored the formation of austenitic cell structure, while slower cooling led to the predominant formation of cellular-dendritic austenite-ferrite (AF) structure.

The presence of austenite cellular and cell-dendritic structures was evidenced in the samples and presented in Fig. 6 and Fig. 10, where the ferrite phase must be expected in the boundaries of the substructure. This result is different from that presented by Katayama and Matsunawa [42]. In their work, the solidification of a stainless steel with 20.6% and 14.8% of Cr_{eq} and Ni_{eq}, respectively, and cooling rates (G.R) from 220 °C/s to 15,500 °C/s, produced a change in the solidification mode from skeleton (FA) to cellular (A). Similar conclusions were made by David et al. [51], who remark that the fully austenitic weld metal structures must be due to a change in the solidification mode to one of primary austenite formation (A mode).

As it is not observed a disagreement between the observed microstructure and those predicted in the map (Fig. 12), it is possible to infer that the cooling rate in this laser cladding process is low and similar to those recorded in conventional fusion welding.

The presence of ferrite is confirmed by the action of ferric chloride, being highlighted as the dark phase, located in both columnar and equiaxial zones (Fig. 5). Therefore, the presence of ferrite involves FA solidification and both regions.

4 Conclusions

In this contribution, laser coating was performed using as substrate an AISI 304 stainless steel and an AISI 316 powder as filler metal.

The shape of the deposited bead is related to the processing parameters. The penetration varies mainly with the laser power and, to a lesser degree, with the powder mass flow because the heat on the substrate is the energy coming from the transmitted beam and from the particles heated by the laser beam inside the interaction area. Regarding the bead height, there is a marked effect of the turntable and the power of the beam, as it allows producing the largest fusion and metal pile-up. Finally, the width of the deposition responds essentially to the laser power when the laser speed is low.

The appearance of face reinforcement depends on the power required to melt the particles (P_{mp}), which is conditioned by its speed, defined through the transport gas flow of the powder.

Macroscopically, the deposits present the formation of banding in addition to two regions in the fusion zone: a columnar zone and a central region with equiaxial grains. Banding is generated by changes in microstructure size,

derived from the local variation in the solidification rate. The growth of the columnar structure from the fusion line toward the deposit surface occurs because this is the direction of maximum temperature gradient. The equiaxial zone corresponds to the column of grain growth parallel to the beam's direction, which gives the appearance of equiaxial grains, and also explains why the size of the equiaxial zone changes with scanning speed.

Microscopically, the columnar zone is characterized by the presence of cellular and dendritic substructure, while in the equiaxial zone cellular, cellular-dendritic, and columnar-dendritic structures are observed. In both regions, the changes are governed mainly by the solidification parameter (G/R), with the microstructure size determined by the cooling rate (G.R), both increasing from the surface to the bottom of the fusion zone.

Availability of data and materials Not applicable.

Author contributions Edwar Andrés Torres López: conceived the idea of evaluating of the band formation; investigated and analyzed the finds of the present work; took the lead in writing the manuscript. Luis Henrique Rodrigues Apolinario: contributed with microstructural analysis, digital image analysis and sample preparation; contributed to the interpretation of the results. Helen Rodrigues Araújo: conducted some SEM characterization of the samples and microstructural analysis; designed the figures and the manuscript formatting. Ivan Bezerra de Mello Picchi: contributed with digital image analysis and sample preparation; performed the measurements and analyzing it. Tiago Felipe de Abreu Santos: supervised the findings of this work; contributed to the interpretation of the results; revised it critically for important intellectual content. All the authors contributed to manuscript writing.

Compliance with ethical standards

Competing interests The authors declare that they have no conflict of interest.

Ethical approval It is approved that the paper is original and has been written based on the authors' own finding. All the figures and tables are original. WRC-1992 diagram (Fig. 11) and Schaeffler diagram (Fig. 12) were adapted to the authors' work, citing original sources, and every expression from other published works were acknowledged and referenced.

Consent to participate All the authors consent to participate.

Consent to publish The authors have consented to the publishing of the present manuscript.

References

1. (2019) London Metal Exchange. In: London Metal Exchange. https://www.lme.com. Accessed 22 Jan 2019
2. Lippold JC, Kotecki DJ (2005) Welding metallurgy and weldability of stainless steels. John Wiley, Hoboken, NJ
3. Lancaster JF (1999) Metallurgy of welding. Elsevier
4. Lippold JC (1994) Solidification behavior and cracking susceptibility of pulsed-laser welds in austenitic stainless steels. Welding Journal Including Welding Research Supplement 73:129s–139s
5. Santos TFA, Andrade MS (2008) Avaliação dilatométrica da reversão das martensitas induzidas por deformação em um aço inoxidável austenítico do tipo ABNT 304. Matéria (Rio de Janeiro) 13:587–596
6. Lee YS, Nordin M, Babu SS, Farson DF (2014) Influence of fluid convection on weld pool formation in laser cladding. Weld J 93:292s–300s
7. Suutala N, Takalo T, Moisio T (1979) The relationship between solidification and microstructure in austenitic and austenitic-ferritic stainless steel welds. Metall Trans A 10:512–514
8. Abe H, Watanabe Y (2008) Low-temperature aging characteristics of type 316L stainless steel welds: dependence on solidification mode. Metall Mater Trans A 39:1392–1398
9. Fu JW, Yang YS (2013) Origin of the lathy ferrite in AISI 304 stainless steel during directional solidification. J Alloys Compd 580:191–194
10. Goodarzi DM, Pekkarinen J, Salminen A (2017) Analysis of laser cladding process parameter influence on the clad bead geometry. Welding in the World 61:883–891
11. Yu T, Yang L, Zhao Y, Sun J, Li B (2018) Experimental research and multi-response multi-parameter optimization of laser cladding Fe313. Opt Laser Technol 108:321–332
12. T-B YU, B-X SONG, W-C XI et al (2019) Parametric study and optimization of Fe-based alloy powder laser cladding of stainless steel. Lasers in Engineering (Old City Publishing) 44:11–31
13. David SA, Babu SS, Vitek JM (2003) Welding: solidification and microstructure. JOM 55:14–20. https://doi.org/10.1007/s11837-003-0134-7
14. Shankar V, Gill TPS, Mannan SL, Sundaresan S (2003) Solidification cracking in austenitic stainless steel welds. Sadhana 28:359–382. https://doi.org/10.1007/BF02706438
15. Tate SB, Liu S (2014) Solidification behaviour of laser welded type 21Cr–6Ni–9Mn stainless steel. Sci Technol Weld Join 19:310–317
16. Soltani HM, Tayebi M (2018) Comparative study of AISI 304L to AISI 316L stainless steels joints by TIG and Nd: YAG laser welding. J Alloys Compd 767:112–121
17. Apolinario LHR, Wallerstein D, Montealegre MA, Urtiga Filho SL, Torres EA, Hermenegildo TFC, Santos TFA (2019) Predominant solidification modes of 316 austenitic stainless steel coatings deposited by laser cladding on 304 stainless steel substrates. Metall and Mat Trans A 50:3617–3628. https://doi.org/10.1007/s11661-019-05293-y
18. Karma A, Sarkissian A (1993) Interface dynamics and banding in rapid solidification. Phys Rev E 47:513–533
19. Sarkissian A, Karma A (1994) On the formation of the banded structure in rapid solidification. Mater Sci Eng A 178:153–157. https://doi.org/10.1016/0921-5093(94)90534-7
20. Conti M (1998) Heat diffusion and banding in rapid solidification. Phys Rev E 58:6166–6172. https://doi.org/10.1103/PhysRevE.58.6166
21. ASTM International (2008) ASTM E3-01, Standard practice for preparation of metallographic specimens
22. Bruck GJ (1987) High-power laser beam cladding. JOM 39:10–13
23. Davim JP, Oliveira C, Cardoso A (2006) Laser cladding: an experimental study of geometric form and hardness of coating using statistical analysis. Proc Inst Mech Eng B J Eng Manuf 220:1549–1554
24. Davim JP, Oliveira C, Cardoso A (2008) Predicting the geometric form of clad in laser cladding by powder using multiple regression analysis (MRA). Mater Des 29:554–557
25. Riveiro A, Mejías A, Lusquiños F, del Val J, Comesaña R, Pardo J, Pou J (2014) Laser cladding of aluminium on AISI 304 stainless steel with high-power diode lasers. Surf Coat Technol 253:214–220
26. Qin GL, Lei Z, Lin SY (2007) Effects of Nd: YAG laser+ pulsed MAG arc hybrid welding parameters on its weld shape. Sci Technol Weld Join 12:79–86
27. Ju J, Zhou Y, Kang M, Wang J (2018) Optimization of process parameters, microstructure, and properties of laser cladding fe-based alloy on 42CrMo steel roller. Materials 11:2061
28. De Oliveira U, Ocelik V, De Hosson JTM (2005) Analysis of co-axial laser cladding processing conditions. Surf Coat Technol 197:127–136
29. Carrard M, Gremaud M, Zimmermann M, Kurz W (1992) About the banded structure in rapidly solidified dendritic and eutectic alloys. Acta Metall Mater 40:983–996
30. Peng L, Taiping Y, Sheng L, Dongsheng L, Qianwu H, Weihao X, Xiaoyan Z (2005) Direct laser fabrication of nickel alloy samples. Int J Mach Tools Manuf 45:1288–1294
31. Zhang K, Wang S, Liu W, Shang X (2014) Characterization of stainless steel parts by laser metal deposition shaping. Mater Des 55:104–119
32. Kurz W, Trivedi R (1996) Banded solidification microstructures. Metall Mater Trans A 27:625–634
33. Gremaud M, Carrard M, Kurz W (1990) The microstructure of rapidly solidified Al- Fe alloys subjected to laser surface treatment. Acta Metall Mater 38:2587–2599
34. Fukumoto S, Kurz W (1999) Solidification phase and microstructure selection maps for Fe-Cr-Ni alloys. ISIJ Int 39:1270–1279
35. Zhong M, Liu W (2010) Laser surface cladding: the state of the art and challenges. Proc Inst Mech Eng C J Mech Eng Sci 224:1041–1060
36. Hemmati I, Ocelik V, De Hosson JTM (2011) Microstructural characterization of AISI 431 martensitic stainless steel laser-deposited coatings. J Mater Sci 46:3405–3414
37. David SA, Vitek JM (1989) Correlation between solidification parameters and weld microstructures. Int Mater Rev 34:213–245. https://doi.org/10.1179/imr.1989.34.1.213
38. Koseki T (2002) Solidification and solidification structure control of weld metals. Weld Int 16:347–365
39. Frenk A, Kurz W (1992) Microstructure formation in laser materials processing. Lasers in Engineering 1:193–212
40. Pei YT, De Hosson JTM (2000) Functionally graded materials produced by laser cladding. Acta Mater 48:2617–2624
41. Lu S-Z, Hunt JD, Gilgien P, Kurz W (1994) Cellular and dendritic growth in rapidly solidified Al- Fe and Al- Cu alloys. Acta Metall Mater 42:1653–1660
42. Katayama S, Matsunawa A (1984) Solidification microstructure of laser welded stainless steels. In: International Congress on Applications of Lasers & Electro-Optics. Laser Institute of America, pp 60–67
43. Kurz W, Trivedi R (1994) Rapid solidification processing and microstructure formation. Mater Sci Eng A 179:46–51
44. Kou S (2003) Welding metallurgy. USA, New Jersey
45. Blecher JJ, Palmer TA, DebRoy T (2014) Solidification map of a nickel-base alloy. Metall Mater Trans A 45:2142–2151
46. Lippold JC (2015) Welding metallurgy and weldability. Wiley Online Library
47. Kotecki DJ, Siewert TA (1992) WRC-1992 constitution diagram for stainless steel weld metals: a modification of the WRC-1988 diagram. Weld J 71:171–178

48. Shahi AS, Pandey S (2006) Prediction of dilution in GMA and UGMA stainless steel single layer cladding using response surface methodology. Sci Technol Weld Join 11:634–640

49. Yoganandh J, Kannan T, Babu SK, Natarajan S (2013) Optimization of GMAW process parameters in austenitic stainless steel cladding using genetic algorithm based computational models. Exp Tech 37:48–58

50. Murugan N, Parmar RS (1997) Stainless steel cladding deposited by automatic gas metal arc welding. Welding Journal-Including Welding Research Supplement 76:391s–402s

51. David SA, Vitek JM, Reed RW, Hebble TL (1987) Effect of rapid solidification on stainless steel weld metal microstructures and its implications on the Schaeffler diagram. Welding Research Supplement 66:289s–300s

52. Elmer JW, Allen SM, Eagar TW (1989) Microstructural development during solidification of stainless steel alloys. MTA 20:2117–2131. https://doi.org/10.1007/BF02650298